Thermoeconomic Analysis of Concentrated Solar Power Plants Based on Supercritical Power Cycles

María José Montes [1,*], Rafael Guedez [2], David D'Souza [1] and José Ignacio Linares [3]

1   E.T.S. Ingenieros Industriales, Universidad Nacional de Educación a Distancia (UNED), C/Juan del Rosal 12, 28040 Madrid, Spain; ddsouza1@alumno.uned.es
2   Department of Energy Technology, KTH Royal Institute of Technology, Brinellvägen 68, 100 44 Stockholm, Sweden; rafael.guedez@energy.kth.se
3   Rafael Mariño Chair on New Energy Technologies, Comillas Pontifical University, Alberto Aguilera 25, 28015 Madrid, Spain; linares@icai.comillas.edu
*   Correspondence: mjmontes@ind.uned.es; Tel.: +34-91-398-64-65

Featured Application: This work is intended as a guide for the design of solar thermal tower plants based on a microchannel radial receiver refrigerated by a pressurised gas, and coupled to a supercritical CO_2 power cycle. The work demonstrates the influence of the receiver configuration on the plant performance and investment costs.

Abstract: Solar thermal power plants are an alternative for the future energy context, allowing for a progressive decarbonisation of electricity production. One way to improve the performance of such plants is the use of supercritical CO_2 power cycles. This article focuses on a solar thermal plant with a central solar receiver coupled to a partial cooling cycle, and it conducts a comparative study from both a thermal and economic perspective with the aim of optimising the configuration of the receiver. The design of the solar receiver is based on a radial configuration, with absorber panels converging on the tower axis; the absorber panels are compact structures through which a pressurised gas circulates. The different configurations analysed keep a constant thermal power provided by the receiver while varying the number of panels and their dimensions. The results demonstrate the existence of an optimal configuration that maximises the exergy efficiency of the solar subsystem, taking into account both the receiver exergy efficiency and the heliostat field optical efficiency. The evolution of electricity generation cost follows a similar trend to that of the exergy efficiency, exhibiting minimum values when this efficiency is at its maximum.

Keywords: solar central receiver; supercritical carbon dioxide; supercritical partial-cooling cycle; solar thermal power plants; exergy efficiency

1. Introduction

The Levelised Cost of Electricity (LCOE) generated by Solar Thermal Power Plants (STPPs) has been reduced by over 50% in the last decade, primarily driven by economies of scale and improvements in the operation and maintenance (O&M) of the plants [1]. However, further research efforts are needed to make the energy provided by STPPs competitive, dispatchable, and safe. In this regard, the Gen3 program [2] proposes the use of supercritical CO_2 (sCO_2) power cycles coupled to solar central receiver systems as a way to increase the overall efficiency; furthermore, four different pathways are identified, depending on the working fluid in the solar receiver. This study focuses on one of these research lines, proposing the use of pressurised CO_2 as Heat Transfer Fluid (HTF) in the solar receiver coupled to a sCO_2 power cycle, as shown in Figure 1.
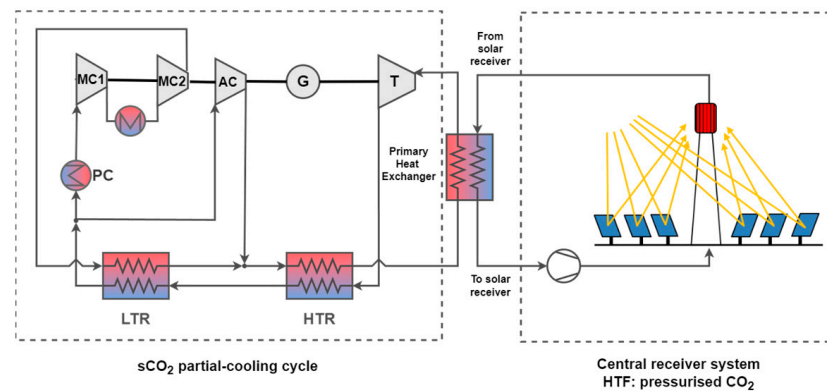
Figure 1. Scheme of a Solar Thermal Power Plant based on a central receiver system working with pressurised CO_2, and indirectly coupled to a sCO$_2$ partial-cooling cycle.

As shown in Figure 1, the STPP under study exhibits an indirect coupling. This is due to the significant differences in operating conditions between the HTF in the solar field (pressurised CO_2) and the power cycle (supercritical CO_2). The primary heat exchanger should be a Printed Circuit Heat Exchanger [3], as this type of heat exchanger performs well under high pressure difference conditions (250 bar in the supercritical cycle compared to 55 bar in the solar receiver).

In STPP schemes with indirect coupling to sCO$_2$ cycles, the working fluid in the solar receiver can be molten salts, with special attention to the new generation of advanced ternary salts [4], a fluidised bed of particles [5], pressurised gas [6], and, finally, liquid metals [7].

Direct coupling STPP schemes are less frequently mentioned in technical literature; in these layouts, the working fluid in the solar receiver is directly supercritical CO_2. Although there are initial studies based on tubular external receivers [8], the large thickness required in the tubes is a challenge to the thermal performance of the receiver. Therefore, an option currently under investigation is the use of receivers based on compact structures [9], and this will be further analysed in this section.

Supercritical power cycles have been extensively studied, mainly for nuclear applications [10] and more recently for solar applications [11]. Within solar applications, notable research includes the study presented by Wang [12], in which different recompression sCO$_2$ cycles are selected and compared based on various criteria, such as cycle efficiency, complexity in terms of additional elements compared to the simplest cycle, and, finally, the sCO$_2$ temperature increase in the primary heat exchanger as it determines the volume of the working fluid to be heated in the solar receiver. A later work [13] specifically compares the conventional recompression cycle with the partial-cooling cycle, with the latter presenting very competitive advantages: higher efficiency, less complexity, and, finally, a significant increase in the sCO$_2$ temperature in the primary heat exchanger, which leads to a smaller solar field with a reduced investment. For this reason, as shown in Figure 1, the chosen power cycle is the partial cooling configuration.

Regarding the solar receiver, there are also different designs to work with pressurised gases or supercritical fluids. This study focuses on microchannel receivers, whose compact structures have been extensively studied for working with these fluids [6,9], highlighting two prototypes. The first prototype has been developed in the Clean Energy Research Center [14] and consists of a 3 MW_{th} cavity receiver. The second has been developed by the National Renewable Energy Laboratory [15] and proposes a 10 MW$_e$ external receiver. In both cases, one of the major challenges is the thermal gradient across the thickness of the compact structure. The materials used for these panels, such as stainless steel and nickel or titanium alloys, can withstand high temperatures, but they have the disadvantage of low thermal conductivity [16]. Additionally, in the case of the external receiver, it is necessary to include a light-trapping geometry to reduce radiation heat loss, which is significant due

to the high working temperatures. For these reasons, a radial receiver is proposed [17], where the absorber panels, consisting of compact structures, converge on the tower axis, as shown in Figure 2.
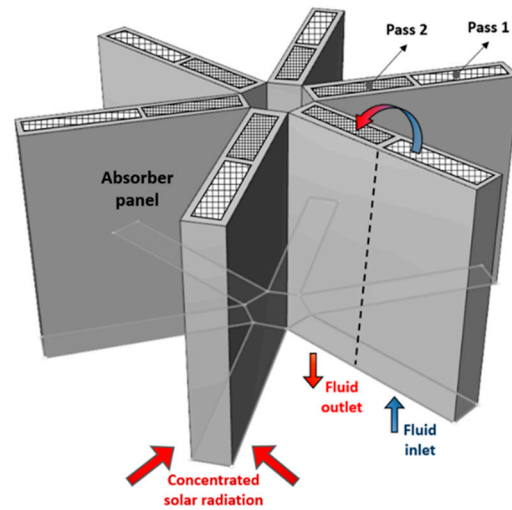
Figure 2. Scheme of the microchannel central solar receiver consisting of compact structures arranged in radial configuration.

This radial configuration allows the absorber panels to be irradiated on both sides, thereby reducing the thermal gradient. In addition, the prism-shaped cavity formed between two consecutive and converging absorber panels acts as a light-trapping geometry, reducing radiation heat loss to the outside. This effect is favoured by the fact that the panel region with the highest surface temperature is the inner part, closer to the tower axis, which has a lower view factor with the cavity aperture, as can be seen in Figure 3a. Lastly, this design uses the concept of increasing compactness, which means that the hydraulic diameter of the channels decreases from one flow pass to the next one as the sCO_2 is heated, as shown in Figure 3b. This approach improves the cooling of the absorber panel in the region subjected to harsher thermal conditions (higher concentrated solar flux and poorer fluid thermal characteristics due to higher temperature) without excessively penalising pressure drop.

(**a**)
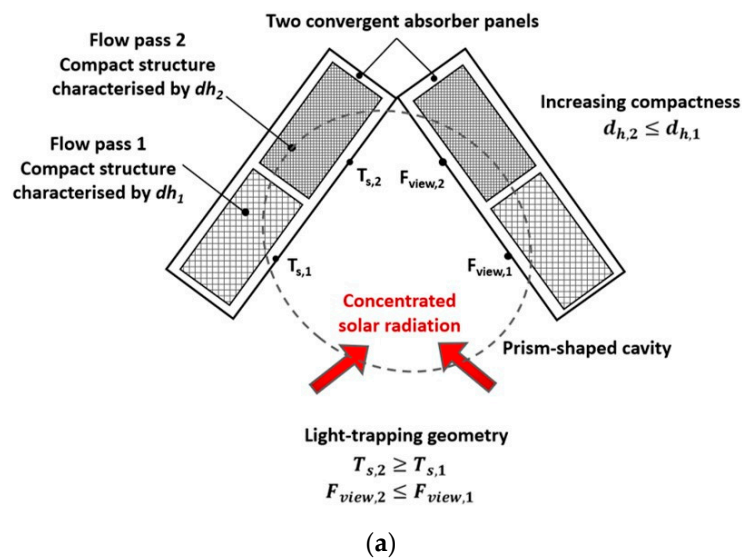
Figure 3. *Cont.*
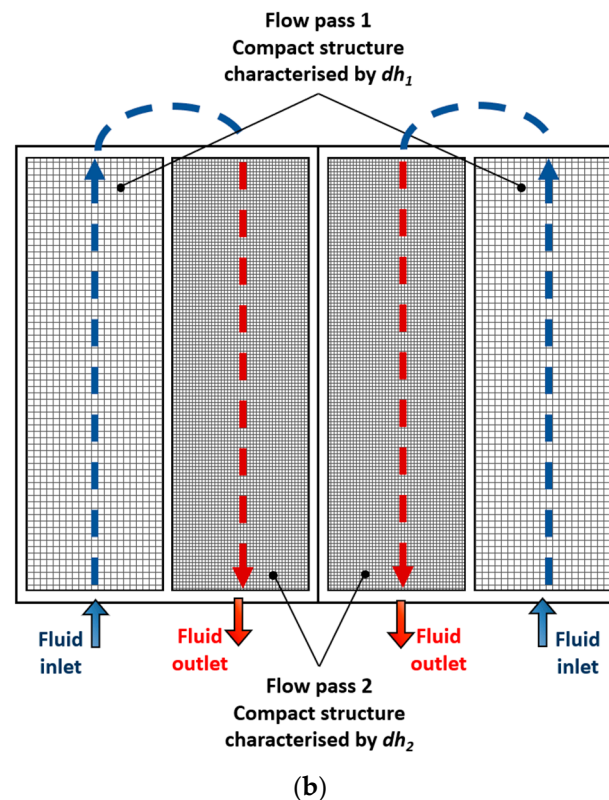
Figure 3. Schemes in use of the microchannel central solar receiver: (**a**) top view of one of the prism-shaped cavities formed between two consecutive and converging absorber panels; (**b**) projected view of one of the prism-shaped cavities, distinguishing in the same absorber panel two fluid flow passes with increasing compactness.

The work is structured as follows: in Section 2, the models used to characterise the supercritical power cycle, the heliostat field, and the solar receiver are explained. These models provide a comprehensive understanding of the previously mentioned systems, allowing for a detailed analysis of their performance and optimisation. The last point of Section 2 proposes the objective functions to be analysed as well as the methodology used. Section 3 presents and discusses the results, providing a scientific explanation for them. Finally, there is a section dedicated to the conclusions.

2. Materials and Methods

2.1. The sCO$_2$ Partial-Cooling Cycle

The sCO$_2$ cycle model includes the thermodynamic analysis of the cycle components, such as the supercritical compressor, the heat exchangers, and the turbine. Various equations and parameters are considered to calculate the efficiency and performance of the cycle, which are implemented in the software Engineering Equation Solver (EES) [18]. The partial cooling layout is depicted in Figure 4.

As shown in Figure 4, the sCO$_2$ partial-cooling cycle is based on the recompression configuration, but it differs from this layout because the Main Compressor (MC) is split in two, introducing an intermediate cooling between the two compressors. Only a portion of the sCO$_2$ is cooled, while another percentage is introduced into the Auxiliary Compressor (AC). The main compressor provides the more pressurised sCO$_2$ stream to the Low Temperature Recuperator (LTR), while the auxiliary compressor connects directly to the High Temperature Recuperator (HTR). Heat is supplied through the Primary Heat Exchanger (PHE), located upstream the Turbine (T). The cycle is refrigerated by an air-cooled Pre-Cooler (PC). The equations governing the behaviour of all the elements of the cycle can

be found in the technical literature [10], so they are not summarised in this article. The thermodynamic properties at each of the points marked in Figure 4 are listed in Table 1.
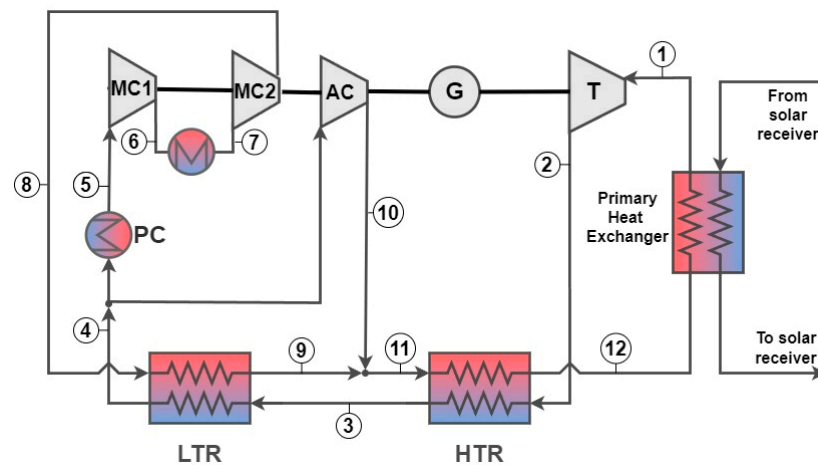
Figure 4. Layout of the sCO$_2$ partial-cooling cycle, indirect coupling configuration, including the state points (1–12). T, Turbine; G, Generator; MC, Main Compressor; AC, Auxiliary Compressor; LTR, Low Temperature Recuperator; HTR, High Temperature Recuperator; PC, pre-cooler.

Table 1. Thermodynamic properties of the state points of simulated partial-cooling cycle (Source: [19]).

State Points	P (bar)	T (°C)	h (kJ/kg)
1	250	688	699.5
2	86.2	545.1	531.4
3	85.8	142.3	62.99
4	85.4	85.38	−12.13
5	85	50	−80.9
6	120.3	77.05	−66.64
7	119.9	50	−170.2
8	251.2	80.18	−147.1
9	250.8	137.1	−26.99
10	250.8	136.3	−28.48
11	250.8	136.8	−27.54
12	250.4	482.8	440.9
Cycle power (MW$_e$)		50	
Source thermal power (MW_{th})		103.42	
Cycle efficiency (%)		48.41	

As seen in Table 1, to generate 50 MW$_e$, the power cycle requires 103.42 MW_{th} from the solar subsystem at the design point. For this analysis, thermal storage has not been considered, although it would be necessary to ensure the dispatchability of the plant. Since the study conducted is under design conditions, considering or not considering thermal storage would involve considering or not considering the additional cost of such storage, which would be the same for all the STPP configurations analysed.

2.2. The Solar Receiver

The solar receiver model describes the thermal behavior of the receiver when exposed to concentrated solar radiation [20]. This model has been implemented in Matlab [21], and the thermofluidodynamic properties of CO$_2$ are provided by the database NIST REF-PROP [22]. The model is based on an energy balance in the direction of fluid heating and a thermal resistance model that characterises the temperature gradient across the panel thickness. The common iteration variable of both models is the temperature at the external surface of the absorber panel, as shown in Figure 5.
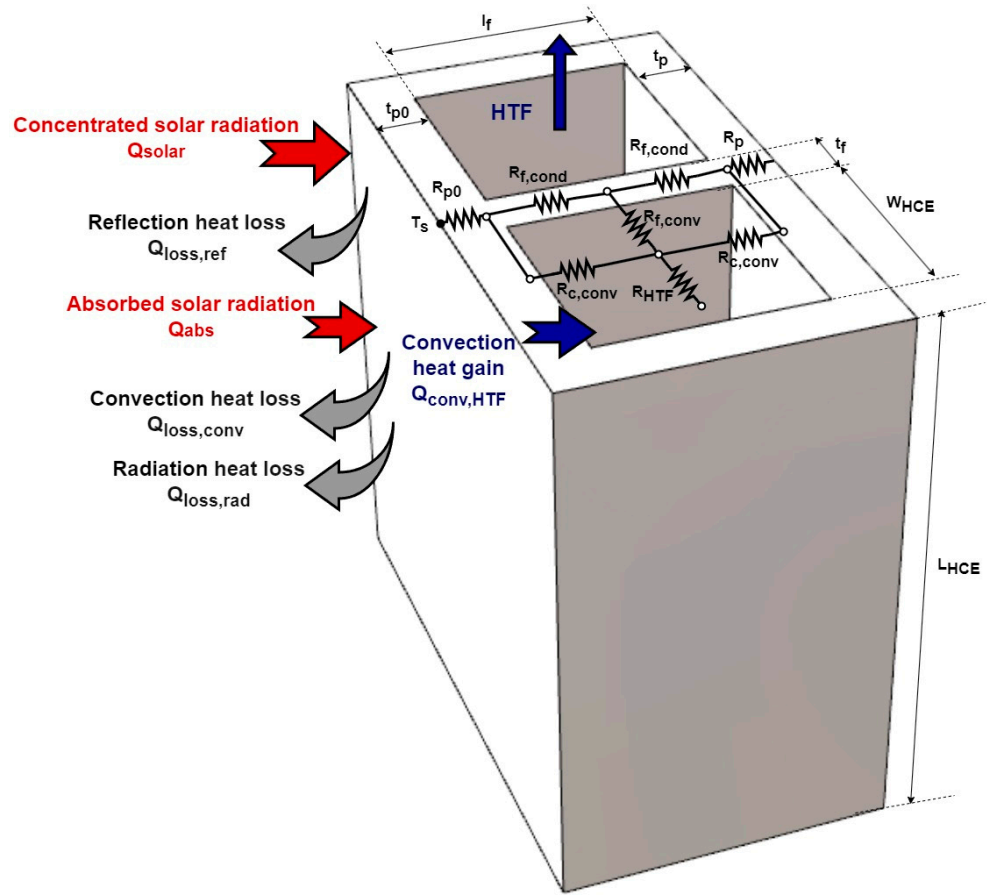
Figure 5. Scheme of the thermal models that characterise the solar receiver performance.

To characterise the fluid heating along the flow direction, it is necessary to divide the channel into Heat Control Elements (*HCEs*), in each of which the fluid properties are assumed to be constant. For each of these *HCEs*, the energy balance is given by Equations (1)–(3).

$$\dot{Q}_{solar}\big|_{HCE} = \dot{Q}_{abs}\big|_{HCE} + \dot{Q}_{loss,ref}\big|_{HCE} \tag{1}$$

$$\dot{Q}_{abs}\big|_{HCE} = \dot{Q}_{conv,HTF}\big|_{HCE} + \dot{Q}_{loss,conv}\big|_{HCE} + \dot{Q}_{loss,rad}\big|_{HCE} \tag{2}$$

$$\dot{Q}_{loss}\big|_{HCE} = \dot{Q}_{loss,rad}\big|_{HCE} + \dot{Q}_{loss,ref}\big|_{HCE} + \dot{Q}_{loss,conv}\big|_{HCE} \tag{3}$$

As observed in Equation (3), the total heat losses are the sum of the radiation, reflection, and convection heat loss. Radiation heat loss is calculated using the simplified formula of Stefan-Boltzmann law [23], accounting for the view factor between the panel external surface and the aperture of the prism-shaped cavity. The reflection loss represents a percentage of the incident heat on the panel, depending on the solar reflectivity, and also includes the view factor. Convection losses are calculated using Siebers and Kraabel correlation [24], which considers both forced convection and free convection.

The thermo-fluid dynamic behavior of the CO_2 is characterised by the convection heat gain and pressure drop in the flow direction. Both effects depend on the fluid regime: laminar, turbulent, or transitional. The equations used for each case are summarised in Table 2.

Table 2. Correlations for the convection heat transfer coefficient and friction factor of the fluid in each heat control element (Source: [3,10]).

Convection Heat Transfer: $\dot{Q}_{conv,\,HTF} = A_{channel} \cdot h_{conv} \cdot \left(T_{si} - T_f \right)$	
Correlation	Validity
$Nu_{Dh} = \frac{(f/8) \cdot (Re_{Dh} - 1000) \cdot Pr}{1 + 12.7 \cdot \left(\sqrt{\frac{f}{8}} \right) \cdot \left(Pr^{2/3} - 1 \right)} \cdot \left(\frac{Pr}{Pr_{si}} \right)^{0.11}$ $f = \left(1.82 \cdot log_{10}(Re_{Dh}) - 1.64 \right)^{-2}$	$5000 \leq Re_{Dh}$
$Nu_{Dh} = 4.089 + \frac{Nu_{Gnielinski}\vert_{Re=5000} - 4.089}{5000 - 2300} \cdot (Re - 2300)$	$2300 < Re_{Dh} < 5000$
$Nu = 4.089$	$Re_{Dh} \leq 2300$
Pressure drop: $\Delta P_{HTF} = \frac{1}{2} \cdot f_D \cdot \left(\frac{L_{HCE}}{D_h} \right) \cdot \rho \cdot u^2,\ \ f_D = 4 \cdot f_F$	
Correlation	Validity
$\frac{1}{f_F} = 1.7372 \cdot \ln\left[\frac{Re_{Dh}}{1.964 \cdot \ln(Re_{Dh}) - 3.8215} \right]$	$10^4 \leq Re_{Dh} \leq 10^7$
$f_F = f_{F,2300} + \frac{(f_F\vert_{Re=10000} - f_F\vert_{Re=2300}) \cdot (Re - 2300)}{10000 - 2300}$	$2300 < Re_{Dh} < 10^4$
$f_F = \frac{16}{Re_{Dh}}$	$Re_{Dh} \leq 2300$

In Table 2, Nu is the Nusselt number; Re_{Dh} is the Reynolds number based on the hydraulic diameter of the duct, D_h; Pr is the Prandtl number at the fluid temperature; Pr_{si} is the Prandtl number based on the duct inner surface temperature; L is the *HCE* length; D_h is the hydraulic diameter of the duct; ρ is the average fluid density; u is the average fluid velocity; and f_D is the Darcy friction factor, which is four times the Fanning friction factor, f_F.

The thermal resistance model across the panel thickness characterises the temperature gradient between parallel channels rows in the direction of concentrated solar flux. The equivalent overall thermal resistance for a panel with a number of parallel channels rows equal to $N_{c,rows}$ is given by Equation (4). The specific value of each of these resistances is given in Table 3.

$$
\begin{aligned}
R_{th,\,panel} = R_{p0,cond} \\
+ \tfrac{N_{c,rows}}{2} \Big[R_{p,cond} \\
+ \Big\{ R_{c,conv} \parallel \Big(R_{f,cond} + \big((R_{f,cond} + R_{c,conv}) \parallel R_{f,conv} \big) \Big) \Big\} \\
+ R_{HTF} \Big]
\end{aligned}
\tag{4}
$$

Table 3. Thermal resistances included in the calculation of the thermal gradient across the panel thickness.

Symbol	Description	Expression
$R_{p,cond}$	Thermal resistance due to conduction through the wall thickness of the intermediate (frontal) plate	$R_{p,cond} = \frac{t_p}{k_{rec} \cdot W_{HCE} \cdot L_{HCE}}$
$R_{c,conv}$	Thermal resistance due to convection between the channel base and top surface	$R_{c,conv} = \frac{1}{h_{conv} \cdot W_{HCE} \cdot L_{HCE}}$
$R_{f,cond}$	Thermal resistance due to conduction through the fin half length	$R_{f,cond} = \frac{\left(\frac{l_f}{2} \right)}{k_{rec} \cdot t_f \cdot L_{HCE}}$
$R_{f,conv}$	Thermal resistance due to convection from the fin surface to the fluid	$R_{f,conv} = \frac{1}{2 \cdot l_f \cdot h_{conv} \cdot L_{HCE}}$
R_{HTF}	Thermal resistance due to the fluid heat gain	$R_{HTF} = \frac{1}{\rho \cdot c_p \cdot u \cdot W_{HCE} \cdot L_{HCE}}$

In Table 3, t_p is the intermediate plate thickness (t_{p0} for frontal plate); t_f and l_f are the fin thickness and length, respectively; and L_{HCE} and W_{HCE} are the *HCE* length and width, respectively. These geometric parameters are also shown in Figure 5. Regarding the thermal parameters: ρ, c_p, and u are the average fluid density, specific heat, and velocity in each *HCE*; k_{rec} is the absorber thermal conductivity; and h_{conv} is the convection heat transfer coefficient to the fluid.

The solar receiver is sized to provide the thermal power required by the power cycle. The optimal CO_2 pressure at the inlet of the receiver is approximately 55 bar [25]. Assuming that the primary heat exchanger is balanced with a Terminal Temperature Difference (TTD) of 12 °C, and that the interconnection pipes are adiabatic, the temperature rise of the CO_2 in the solar receiver ranges from 494.8 °C to 700 °C.

This solar receiver model has been validated [20] with data from a Thermal Resistance Model (TRM) and a Computational Fluid Dynamics (CFD) model and some limited experimentation [26].

2.3. The Heliostat Field

The heliostat field is circular, as in the case of the external receivers. The heliostat field was modelled using two open-source software tools developed by NREL: SolarPilot [27] and SolTrace [28]. SolarPilot is used for heliostat layout optimization and economic analysis, while SolTrace is employed for detailed ray tracing and optical analysis of the heliostat field.

SolarPilot has been used to obtain the optimal heliostats layout based on the design point, the thermal power, the tower height, and the receiver configuration, which is different for each of the STPPs in the comparative analysis. The design point is set as solar noon on 21 March in Seville (37.4 N, 5.9 W), Spain. The Direct Normal Irradiation (DNI) is equal to 950 W/m^2, the ambient temperature is 25 °C, and the wind velocity is 2 m/s. The thermal power is 103.42 MW_{th} in all the configurations, because the sCO$_2$ cycle is the same in all the STPPs analysed. The tower height, equal to 109 m, has been calculated based on the thermal power using Equation (5) [29]:

$$H_{tower} = 0.2552 \cdot \dot{Q}_{th,receiver}(MW_{th}) + 82.6 \qquad (5)$$

The heliostats chosen for this calculation are the default ones in SolarPilot, and their main characteristics are shown in Table 4.

Table 4. Geometric ang optic characteristics of the heliostats.

Heliostat Geometry and Focusing	
Structure width (m) × height (m)	12.2 × 12.2
N. of horizontal panels	2
N. of vertical panels	8
Focusing type	At slant
Optical error parameters	
Elevation pointing error (rad)	0
Azimuth pointing error (rad)	0
Surface slope error in X/Y (mrad)	1.53
Reflected beam error in X/Y (mrad)	0.2
Mirror performance parameters	
Reflective surface ratio	0.97
Mirror reflectivity	0.95
Soiling factor	0.95

For each STPP analysed, the heliostat field obtained with SolarPilot has been exported to SolTrace in order to perform a detailed ray tracing calculation of the solar flux map on each absorber panel and the optical efficiency. As will be seen in Section 3, the number

of heliostats will vary depending on the receiver thermal performance and the solar field optical efficiency, which directly impacts the cost.

2.4. The Comparative Analysis as Function of the Receiver Configuration

The comparative analysis is based on different receiver configurations, keeping the receiver thermal power constant. The CO_2 temperature at the receiver inlet and outlet as well as the CO_2 pressure at the receiver inlet are also constant, as well as the geometric characteristics of the compact structure inside the panel, as shown in Table 5.

Table 5. Geometric and thermo-fluid dynamic parameters of the solar receiver that remain constant in the comparative analysis.

Global Receiver Parameters	
Thermal power (MW_{th})	103.42
CO_2 temperature at the receiver inlet (°C)	494.8
CO_2 temperature at the receiver outlet (°C)	700
CO_2 pressure at the receiver inlet (bar)	55
Compact structure parameters	
Pass 1	
Channel dimensions (mm $\times$ mm)	10×10
Number of channel rows	6
Plate thickness (mm)	1
Frontal/back plate thickness (mm)	1.5
Thickness between channels (mm)	3
Average fluid velocity (m/s)	15
Pass 2	
Channel Dimensions (mm $\times$ mm)	5×5
Number of channel rows	6
Plate thickness (mm)	1
Frontal/back plate thickness (mm)	1.5
Thickness between channels (mm)	3
Average fluid velocity (m/s)	30

By keeping the previous characteristics constant, a comparative analysis can be conducted to evaluate the performance of the solar receiver under different number and size of the absorber panel by means of the following parameters: the energy and exergy efficiencies referred to the receiver, the solar subsystem, and the solar thermal power plant (Equations (6)–(10)). This type of analysis, including both energy and exergy efficiencies, is very useful for analysing STPPs, particularly when the working fluid in the solar receiver is a gas, and pressure drop is therefore an important factor to consider [30,31].

$$\eta_{en,\ receiver} = \frac{\dot{Q}_{conv,CO2,\ receiver}}{\dot{Q}_{solar,receiver}} \tag{6}$$

$$\eta_{ex,receiver} = \frac{\Delta Ex_{CO2,receiver}}{\Delta Ex_{solar,receiver}} \tag{7}$$

$$\eta_{en,\ solar\_subsystem} = \eta_{opt} \cdot \eta_{th,\ receiver} \tag{8}$$

$$\eta_{ex, \ solar\_subsystem} = \eta_{opt} \cdot \eta_{ex, \ receiver} \tag{9}$$

$$\eta_{en, \ STPP} = \eta_{opt} \cdot \eta_{en, \ solar\_subsystem} \cdot \eta_{\ cycle} \tag{10}$$

In previous equations, $\dot{Q}_{conv,CO2,receiver}$ is the total heat gain by convection in the receiver; $\dot{Q}_{solar,receiver}$ is the concentrated solar radiation incident on the receiver; $\Delta Ex_{CO2,receiver}$ is the total exergy gain in the receiver; $\Delta Ex_{solar,receiver}$ is the exergy associated to the solar radiation incident on the receiver, given by Parrot equation [32]; η_{opt} is the optical efficiency of the heliostat field; and η_{cycle} is the thermal efficiency of the sCO$_2$ cycle, equal to 48.41% in all the cases, as seen in Table 1.

The comparative analysis will be conducted from a thermal and optical perspective in Section 3.1, while an economic analysis will be performed in Section 3.2.

3. Results

3.1. Thermal and Optical Analysis of the Solar Thermal Power Plant as a Function of the Receiver Configuration

The results presented in this section only refer to the optical and thermal performance of STPPs that differ in the receiver configuration (number of panels and their dimensions) but that have the same thermal power, as well as the other parameters enumerated in Section 2.4. Table 6 shows the panel dimensions, heat losses, and pressure drop as a function of the number of panels in the receiver.

Table 6. Panel dimensions, heat losses, and pressure drop as function of the number of panels in the receiver, while keeping the receiver thermal power constant.

Number of Panels	Panel Height (m)	Panel Width (m)	Heat Losses (kW$_{th}$)	Pressure Drop (bar)
6	9.153	6.538	2231.465	5.531
7	7.886	5.633	1490.491	4.750
8	6.937	4.955	1066.124	4.159
9	6.202	4.430	806.335	3.700
10	5.618	4.013	636.138	3.343
11	5.138	3.670	520.657	3.046
12	4.739	3.385	436.343	2.798
14	4.0852	2.918	312.163	2.4
16	3.5756	2.554	234.591	2.102

As observed in Table 6, as the number of panels increases, their dimensions decrease. This ultimately leads to higher optical loss due to spillage, which decreases the optical efficiency, as observed in Figure 6a,b. On the other hand, heat losses decrease as the number of panels increases, as the view factor from the panel to the outside decreases due to a reduction in the aperture of the prism-shaped cavity. The pressure drop also decreases because the parallel fluid circuits increase as the number of panels increases, while their length, specifically the panel height, decreases. As a result, both the receiver energy and exergy efficiency improve with an increasing number of absorber panels. The overall solar subsystem performance, which is the convolution of the solar field optical efficiency and the receiver energy/exergy efficiency, exhibits maximum values for configurations between 8 and 10 panels, approximately, as observed in Figure 6a,b.
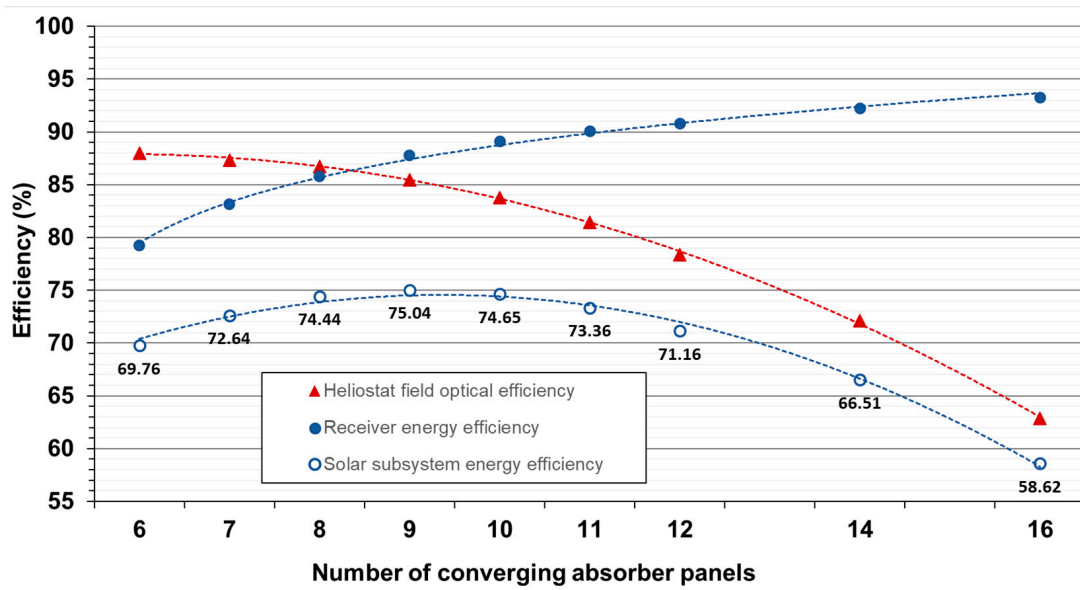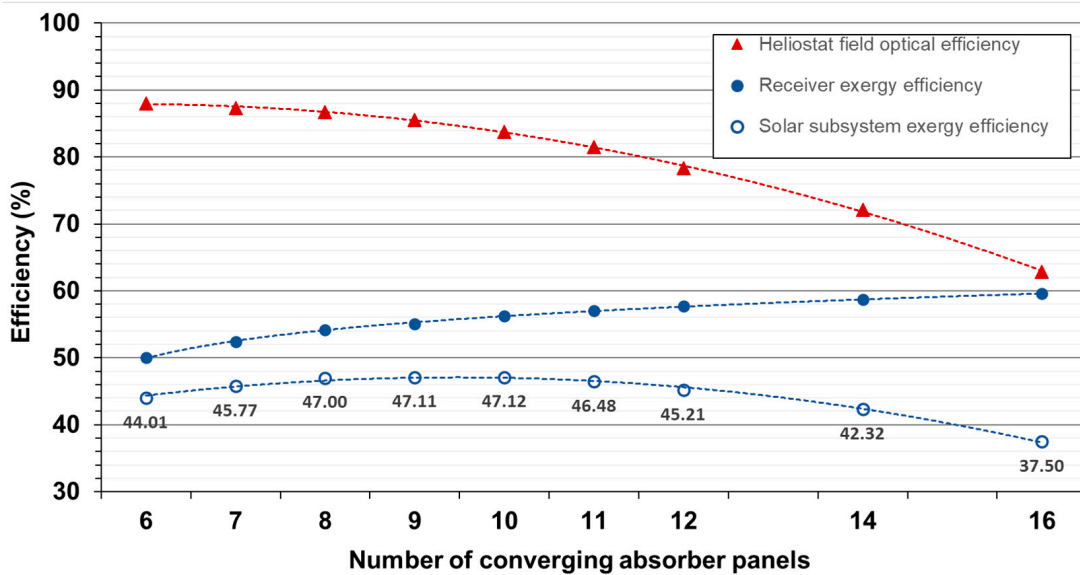
Figure 6. Thermal and optical performance of the receiver and the entire solar subsystem: (**a**) evolution of the optical and energy efficiencies as function of the number of absorber panels while keeping the receiver thermal power constant; (**b**) evolution of the optical and exergy efficiencies as function of the number of absorber panels while keeping the receiver thermal power constant.

Finally, Figure 7 displays the overall energy efficiency of each STPP considered, which follows the same trend as the energy efficiency of the solar subsystem, since the power cycle efficiency is the same for all the configurations analysed: 48.41%, as seen in Table 1. As expected, there is also a maximum efficiency between 8 and 10 panels, which is the result of two opposing effects: on the one hand, energy and exergy efficiency, which increase as the number of panels increases, as heat loss and fluid pressure drop decrease due to shorter parallel circuits; on the other hand, there is a reduction in optical efficiency as the number of panels increases as the spillage loss increases.
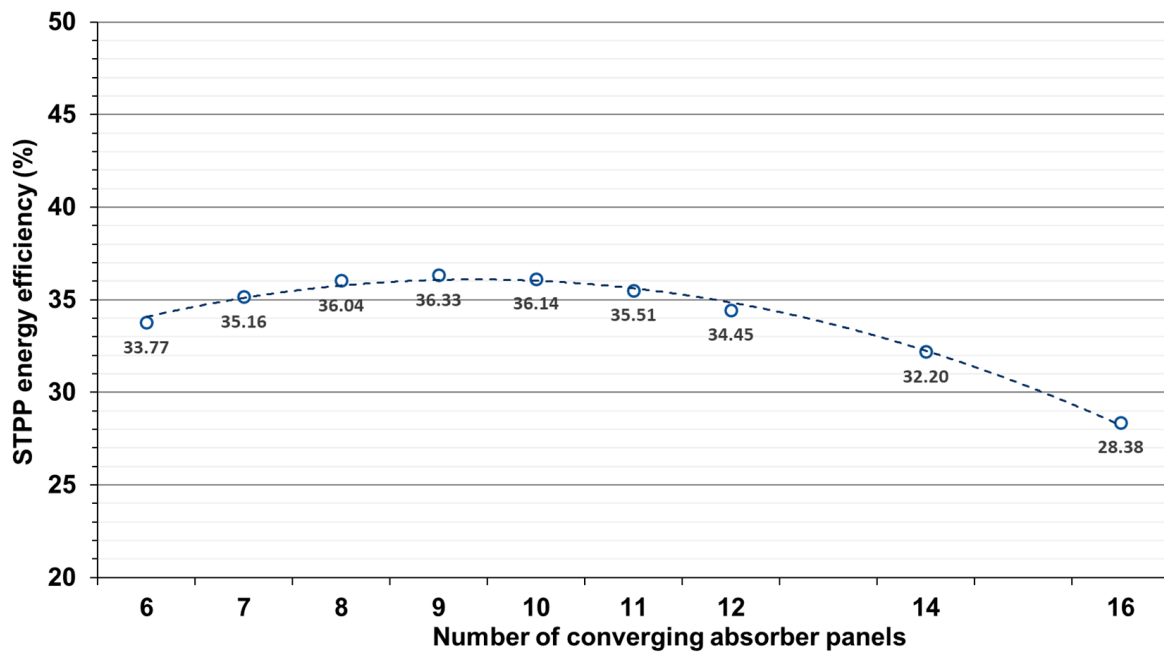
Figure 7. Evolution of the overall energy efficiency of the STPP, as function of the number of absorber panels.

3.2. Economic Analysis of the Solar Thermal Power Plant as a Function of the Receiver Configuration

A comparative economic analysis of the entire STPP has been conducted for each receiver configuration considered in the previous section. For this purpose, the Total Capital Cost (*TCC*) [33], the Payback period (*PB*) [34,35], and the Levelised Cost of Electricity (LCOE) [33] of each STPP have been estimated.

The *PB* is the length of time that it takes to recover the initial capital investment in a project, and it is calculated by means of Equation (11).

$$PB = \frac{TCC}{AEP \cdot (CE - OMC)} \tag{11}$$

In Equation (11), *AEP* is the Annual Electricity Production, which is estimated assuming that the plant has a Capacity Factor (CF) of 25%, as it is a stand-alone CSP plant [36]. Based on this, the annual production for all plants is equal to $109.5 \cdot 10^3$ MWh$_e$/year. *CE* is the electricity cost, 124.9 \$/MWh$_e$, which is based on the average market price at USA [37]. Finally, *OMC* is the O&M costs per MWh$_e$, taken as 23 \$/MWh$_e$ [1].

The LCOE is calculated using Equation (12):

$$LCOE = \frac{CRF \cdot TCC}{AEP} + OMC \tag{12}$$

In Equation (12), *CRF* (%) is the Capital Recovery Factor, calculated as Equation (12):

$$CRF = \frac{WACC \cdot (1 + WACC)^n}{(1 + WACC)^n - 1} . \tag{13}$$

In Equation (13), *WACC* refers to the Weighted Average Capital Cost, which is assumed to be 8%; and *n* represents the economic lifetime, which is assumed to be 30 years. With the aforementioned values, the *CRF* is calculated to be 0.088 years^{-1}.

The *TCC* of the sCO_2 partial-cooling cycle has been calculated using the methodology described in [38,39]. Table 7 summarises the *TCC* for the primary heat exchanger, recuperators, precooler, and turbomachinery. This *TCC* is constant for all the STPPs analysed in the previous section, as the power cycle is the same for all of them.

Table 7. Summary of the total capital cost for each component of the partial-cooling sCO_2 cycle.

Components	Total Capital Cost (Mio.$)
Primary heat exchanger	9.141
Recuperators (LTR + HTR)	20.7
Precooler CO_2/Air	11.8
Turbomachinery (TM)	43
Power cycle	84.641

The *TCC* of the solar field has been calculated according to the equations and reference values provided in the SolarPilot program. The most significant costs are associated with the heliostat field, the receiver, and the tower, as shown in Equations (14)–(16):

$$c_{heliostat,total} = c_{heliostat} \cdot A_{sf} \tag{14}$$

$$c_{rec} = c_{rec,ref} \cdot \left(\frac{A_{rec}}{A_{rec,ref}} \right)^{k_{rec}} \tag{15}$$

$$c_{tower} = c_{tower,fixed} \cdot e^{k \cdot h_{tower}} \tag{16}$$

In the previous equations, $c_{heliostat}$ is the cost of the heliostat per square meter of heliostat reflective area, with a default value in SolarPilot of 145 $/m^2; A_{sf} is the total reflective area in the field, which depends on the number of heliostats in each STPP; $c_{rec,ref}$ is the receiver reference cost, with a default value in SolarPilot of 103 Mio. $; $A_{rec,ref}$ is the receiver reference area, with a default value in SolarPilot of 1571 m^2; k_{rec} is the receiver cost scaling exponent, equal to 0.7 in SolarPilot; A_{rec} is the receiver area, which depends on the number of absorber panels and their size; $c_{tower,fixed}$ is the fixed tower cost, with a default value in SolarPilot of 3 Mio. $; k is the tower cost scaling exponent, equal to 0.0113 in SolarPilot; and h_{tower} is the tower height, equal to 109 m for all the cases analysed.

As seen in Table 8, as the number of absorber panels increases, the receiver area decreases, and, consequently, its cost decreases, since its energy and exergy efficiencies increase, as discussed in the previous section. The tower height and its cost are constant, while the total reflective area increases as the receiver size decreases because of the larger optical losses due to spillage. Although initially reducing the receiver area improves the overall STPP performance, beyond a certain number of absorber panels, the optical efficiency decreases significantly, and the additional investment cost in the solar field does not compensate for the savings in the receiver cost. In the specific example being studied, this occurs from 14 panels onwards, although it will depend on the reference cost and the values adopted for the different parameters.

Finally, Table 9 shows the *PB* and the LCOE for all the STPPs considered. As expected, the *PB* is minimal for the plant with the lowest *TCC*, as *AEP* and *OMC* are the same for all plants. Although this *PB* is high for standard projects, it is in line with other STPPs, and it should be noted that the economic lifetime is 30 years. The LCOE follows an opposite trend compared to the solar subsystem *TCC*, which is logical, since the power cycle *TCC* is the same for all plants as well as the annual estimate of electricity produced.

Table 8. Summary of the total capital cost of the solar subsystem of each solar thermal power plant, based on a partial-cooling sCO_2 cycle.

	Number of Converging Absorber Panels								
	6	7	8	9	10	11	12	14	16
Design parameters									
Tower height (m)	109	109	109	109	109	109	109	109	109
Receiver absorber area (m^2)	718.123	621.922	549.965	494.547	450.917	414.842	384.996	333.777	292.227
Number of heliostats	1243	1245	1259	1269	1294	1339	1401	1566	1869
Economic parameters									
Tower cost (Mio. $)	10.281	10.281	10.281	10.281	10.281	10.281	10.281	10.281	10.281
Receiver cost (Mio. $)	59.546	53.843	49.402	45.863	42.991	40.554	38.489	34.828	31.733
Site improvements cost (Mio. $)	2.871	2.875	2.910	2.930	2.989	3.093	3.236	3.617	4.317
Heliostat field cost (Mio. $)	26.021	26.063	26.356	26.560	27.089	28.031	29.329	32.783	39.126
Contingency cost (Mio. $)	4.210	4.052	4.620	4.355	4.18	4.069	4.031	4.115	4.46
Total direct cost (Mio. $)	102.929	97.114	93.569	89.989	87.530	86.028	85.366	85.624	89.917
Land cost (Mio. $)	2.842	2.812	2.930	2.876	2.889	2.956	3.075	3.443	4.314
Sales tax cost (Mio. $)	2.574	2.477	2.940	2.778	2.671	2.606	2.59	2.654	2.899
Total indirect cost (Mio. $)	5.416	5.289	5.870	5.654	5.560	5.562	5.665	6.097	7.213
Total capital cost (Mio. $)	108.345	102.403	99.439	95.643	93.090	91.590	91.031	91.721	97.130

Table 9. Summary of the total capital cost and levelised cost of energy of each solar thermal power plant, based on a partial-cooling sCO_2 cycle.

	Number of Converging Absorber Panels								
	6	7	8	9	10	11	12	14	16
Solar subsystem *TCC* (Mio.$)	108.345	102.403	99.439	95.643	93.090	91.590	91.031	91.721	97.130
Power cycle *TCC* (Mio.$)	84.641	84.641	84.641	84.641	84.641	84.641	84.641	84.641	84.641
Annual electricity production (GWh_e)	109.5	109.5	109.5	109.5	109.5	109.5	109.5	109.5	109.5
Payback period (*PB*) (years)	11.916	11.549	11.366	11.132	10.974	10.882	10.847	10.890	11.224
Levelised Cost of Energy (LCOE) ($/kWh_e$)	0.178	0.150	0.148	0.145	0.143	0.142	0.141	0.142	0.146

4. Conclusions

This work focuses on the study of a STPP configuration that is included in the new generation of STPPs, aiming to reduce costs through improved performance by employing supercritical power cycles [2].

Specifically, this STPP is based on a central solar receiver refrigerated by a pressurised gas and coupled to a supercritical power cycle. Compared to more conventional configurations of the aforementioned scheme, this STPP presents two innovative elements. Firstly, the power cycle is a SCO_2 partial-cooling layout, which presents significant advantages compared to conventional recompression, such as lower investment due to the smaller recuperator volume, higher thermal efficiency, and higher temperature increment of the sCO_2 in the primary heat exchanger. This leads to a smaller volume of gas to be heated in the receiver, which directly reduces the receiver sizing and the solar field cost. Secondly, the STPP features a novel receiver design based on compact structures in a radial configuration. This design is particularly suitable for working with pressurised gas.

The comparative analysis conducted in this study involves keeping a constant thermal power supplied by the solar receiver while varying its design through the number and dimensions of the absorber panels. The analysis demonstrates that there is an optimal configuration that balances two opposing effects: the increase in receiver thermal efficiency as the number of absorber panels increases, and the decrease in optical efficiency due to increased spillage as the receiver size is reduced. Although this optimum will depend on the specific working conditions chosen, it provides an idea of the range in which the solar thermal plant operates optimally, resulting in lower electricity generation costs.

In the specific case under study, the optimal energy and exergy efficiency is achieved with around 10–12 panels, while the configuration with the minimum LCOE corresponds to 14 panels. This result depends on the reference values and other parameters assumed for the economic study. In any case, the obtained LCOE values are of the same order as the currently estimated values [1], and it is expected that these values will further decrease as economies of scale are developed for these STPPs.

Future lines of work include a more detailed study of the annual analysis, considering transients, startups, and shutdowns. This will involve examining the behavior of the plant throughout the year and optimising its performance under different operating conditions. Additionally, the study aims to explore the integration of thermal energy storage systems within the STPP. This will investigate the feasibility and the benefits of incorporating storage technologies in order to enhance the dispatchability and flexibility of the solar thermal power plant. Furthermore, a more detailed optimisation study of specific components is planned, such as the solar receiver and the primary heat exchanger.

5. Patents

Montes, M.J., Rovira, A., González-Aguilar, J. and Romero, M., 2022. Solar receiver consisting of absorber panels based on compact structures. Spanish Patent ES2911108. PCT application n. PCT/ES2022/070705. Eu. application n. 2023/10572.

Author Contributions: Conceptualization, M.J.M. and R.G.; methodology, M.J.M. and R.G.; software, M.J.M., J.I.L. and D.D.; validation, J.I.L. and D.D.; formal analysis, M.J.M.; investigation, M.J.M., J.I.L. and D.D.; resources, M.J.M., J.I.L. and D.D.; data curation, J.I.L. and D.D.; writing—original draft preparation, M.J.M.; writing—review and editing, R.G., J.I.L. and D.D.; visualization, M.J.M.; supervision, M.J.M.; project administration, M.J.M.; funding acquisition, M.J.M. and J.I.L. All authors have read and agreed to the published version of the manuscript.

Funding: This research was funded by the Spanish Ministry: Ministerio de Economía y Competitividad through the PID2019-110283RB-C31 and PID2019-110283RB-C33 projects.

Data Availability Statement: The data presented in this study are available on request from the corresponding author. The data are not publicly available due to privacy.

Conflicts of Interest: The authors declare no conflict of interest. The funders had no role in the design of the study; in the collection, analyses, or interpretation of data; in the writing of the manuscript; or in the decision to publish the results.

References

1. IRENA. *Renewable Power Generation Costs in 2021*; International Renewable Energy Agency: Abu Dhabi, United Arab Emirates, 2022; ISBN 978-92-9260-452-3.
2. Mehos, M.; Turchi, C.; Vidal, J.; Wagner, M.; Ma, Z.; Ho, C.; Kolb, W.; Andraka, C.; Kruizenga, A. *Concentrating Solar Power Gen3 Demonstration Roadmap (No. NREL/TP-5500-67464, 1338899)*; National Renewable Energy laboratory: Golden, CO, USA, 2017. [CrossRef]
3. Hesselgreaves, J.E. *Compact Heat Exchangers: Selection, Design, and Operation*, 2nd ed.; Elsevier/BH: Amsterdam, The Netherlands, 2017.
4. Turchi, C.S.; Vidal, J.; Bauer, M. Molten salt power towers operating at 600–650 °C: Salt selection and cost benefits. *Sol. Energy* **2018**, *164*, 38–46. [CrossRef]
5. Ho, C. A review of high-temperature particle receivers for concentrating solar power. *Appl. Therm. Eng.* **2016**, *109*, 958–969. [CrossRef]
6. Li, Q.; Tourville, N.G.d.; Yadroitsev, I.; Yuan, X.; Flamant, G. Micro-channel pressurized-air solar receiver based on compact heat exchanger concept. *Sol. Energy* **2013**, *91*, 186–195. [CrossRef]
7. De la Calle, A.; Bayon, A.; Pye, J. Techno-economic assessment of a high-efficiency, low-cost solar-thermal power system with sodium receiver, phase-change material storage, and supercritical CO_2 recompression Brayton cycle. *Sol. Energy* **2020**, *199*, 885–900. [CrossRef]
8. Ho, C.K.; Iverson, B.D. Review of high-temperature central receiver designs for concentrating solar power. *Renew. Sustain. Energy Rev.* **2014**, *29*, 835–846. [CrossRef]
9. Li, Q.; Flamant, G.; Yuan, X.; Neveu, P.; Luo, L. Compact heat exchangers: A review and future applications for a new generation of high temperature solar receivers. *Renew. Sustain. Energy Rev.* **2011**, *15*, 4855–4875. [CrossRef]
10. Dostal, V.A. *Supercritical Carbon Dioxide Cycle for Next Generation Nuclear Reactors*; Massachusetts Institute of Technology (MIT): Cambridge, MA, USA, 2004.

11. Reyes-Belmonte, M.A.; Guédez, R.; Montes, M.J. Bibliometric Analysis on Supercritical CO$_2$ Power Cycles for Concentrating Solar Power Applications. *Entropy* **2021**, *23*, 1289. [CrossRef] [PubMed]

12. Wang, K.; He, Y.L.; Zhu, H.H. Integration between supercritical CO$_2$ Brayton cycles and molten salt solar power towers: A review and a comprehensive comparison of different cycle layouts. *Appl. Energy* **2017**, *195*, 819–836. [CrossRef]

13. Neises, T.; Turchi, C. Supercritical carbon dioxide power cycle design and configuration optimization to minimize levelized cost of energy of molten salt power towers operating at 650 °C. *Sol. Energy* **2019**, *181*, 27–36. [CrossRef]

14. Besarati, S.M.; Goswami, D.Y.; Stefanakos, E.K. Development of a Solar Receiver Based on Compact Heat Exchanger Technology for Supercritical Carbon Dioxide Power Cycles. *J. Sol. Energy Eng.* **2015**, *137*, 031018. [CrossRef]

15. Sullivan, S.D.; Kesseli, J.; Nash, J.; Farias, J.; Kesseli, D.; Caruso, W. *High-Efficiency Low-Cost Solar Receiver for Use Ina a Supercritical CO$_2$ Recompression Cycle (No. DOE-BRAYTON--0005799, 1333813)*; Brayton Energy, LLC: Portsmouth, NH, USA, 2016. [CrossRef]

16. Li, X.; Kininmont, D.; Le Pierces, R.; Dewson, S.J. *Alloy 617 for the High Temperature Diffusion-Bonded Compact Heat Exchangers*; American Nuclear Society—ANS: Downers Grove, IL, USA, 2008.

17. Montes, M.J.; Rovira, A.; González-Aguilar, J.; Romero, M. Solar Receiver Consisting of Absorber Panels Based on Compact Structures. Spanish Patent ES2911108; PCT application n. PCT/ES2022/070705; Eu. application n. 2023/10572. Filed, 22 December 2021.

18. Klein, S.A.; Nellis, G.F. *Mastering EES, F-Chart Software*, (versions 9.373 and newer) 63rd ed.; F-Chart Software LLC: Madison, WI, USA, 2022; Available online: http://www.fchartsoftware.com/ees/mastering-ees.php (accessed on 1 June 2023).

19. Montes, M.J.; Linares, J.I.; Barbero, R.; Rovira, A. Proposal of a new design of source heat exchanger for the technical feasibility of solar thermal plants coupled to supercritical power cycles. *Sol. Energy* **2020**, *211*, 1027–1041. [CrossRef]

20. D'Souza, D.; Montes, M.J.; Romero, M.; González-Aguilar, J. Energy and exergy analysis of microchannel central solar receivers for pressurised fluids. *Appl. Therm. Eng.* **2023**, *219*, 119638. [CrossRef]

21. MATLAB & Simulink—MathWorks, 2022. Available online: https://matlab.mathworks.com (accessed on 1 June 2023).

22. NIST Database. Available online: https://webbook.nist.gov/chemistry/ (accessed on 1 June 2023).

23. Siegel, R.; Howell, J.R. *Thermal Radiation Heat Transfer*, 4th ed.; Taylor & Francis: New York, NY, USA, 2002.

24. Siebers, D.; Kraabel, J. *Estimating Convective Energy Losses from Solar Central Receivers (No. SAND-84-8717, 6906848, ON: DE84010919)*; Sandia National Laboratory: Livermore, CA, USA, 1984. [CrossRef]

25. Montes, M.J.; D'Souza, D.; Linares, J.I.; González-Aguilar, J.; Rovira, A.; Romero, M. Proposal of a Microchannel Receiver for Pressurised Fluids Based on Different Compact Geometries. In Proceedings of the SOLARPACES 2022: International Conference on Concentrating Solar Power and Chemical Energy Systems, Albuquerque, NM, USA, 26–30 September 2022.

26. Lei, N. The Thermal Characteristics of Multilayer Minichannel Heat Sinks in Single-Phase and Two-Phase Flow. Ph.D. Thesis, The University of Arizona (US), Tucson, AZ, USA, 2006.

27. Wagner, M.J.; Wendelin, T. SolarPILOT: A power tower solar field layout and characterization tool. *Sol. Energy* **2018**, *171*, 185–196. [CrossRef]

28. Wendelin, T. SolTRACE: A New Optical Modeling Tool for Concentrating Solar Optics. In Proceedings of the ISEC 2003: International Solar Energy Conference, Kohala Coast, HI, USA, 15–18 March 2003; American Society of Mechanical Engineers: New York, NY, USA, 2003; NREL Report No. CP-550-32866; pp. 253–260.

29. Stalin Maria Jebamalai, J. Receiver Design Methodology for Solar Tower Power Plants. Master's Thesis, KTH School of Industrial Engineering and Management, Stockholm, Sweden, 2016. Available online: http://urn.kb.se/resolve?urn=urn:nbn:se:kth:diva-192664 (accessed on 1 June 2023).

30. Aligholami, M.; Khosroshahi, S.S.; Khosroshahi, A.R. Hydrodynamic and thermodynamic enhancement of a solar chimney power plant. *Sol. Energy* **2019**, *191*, 180–192. [CrossRef]

31. Bejan, A.; Tsatsaronis, G.; Moran, M. *Thermal Design & Optimization*; Wiley: Hoboken, NJ, USA, 1996.

32. Parrott, J.E. Theoretical upper limit to the conversion efficiency of solar energy. *Sol. Energy* **1978**, *21*, 227–229. [CrossRef]

33. Short, W.; Packey, D.J.; Holt, T. *A Manual for the Economic Evaluation of Energy Efficiency and Renewable Energy Technologies*; National Renewable Energy Laboratory: Golden, CO, USA, 2013; p. 1995. [CrossRef]

34. Shafiee, M.; Alghamdi, A.; Sansom, C.; Hart, P.; Encinas-Oropesa, A. A Through-Life Cost Analysis Model to Support Investment Decision-Making in Concentrated Solar Power Projects. *Energies* **2020**, *13*, 1553. [CrossRef]

35. Schlaifer, P. Performance Calculations and Optimisation of a Fresnel Direct Steam Generation CSP Plant with Heat Storage. Ph.D. Thesis, KTH Industrial Engineering and Management, Stockholm, Sweden, 2012.

36. Islam, T.; Huda, N.; Abdullah, A.B.; Saidur, R. A comprehensive review of state-of-the art concentrating solar power (CSP) technologies: Current status and research trends. *Renew Sustain. Energy Rev.* **2018**, *91*, 987–1018. [CrossRef]

37. Energy Information Administration. Electric Power Annual 2023. Average Retail Price of Electricity to Ultimate Consumers by End-Use Sector. 2023. Available online: www.eia.doe.gov (accessed on 1 June 2023).

38. Fleming, D.D.; Conboy, T.M.; Pasch, J.J.; Wright, S.A.; Rochau, G.E.; Fuller, R.L. *Scaling Considerations for a Multi-Megawatt Class Supercritical CO$_2$ Brayton Cycle and Commercialization*; No. SAND2013-9106, 1111079; Sandia National Laboratory: Livermore, CA, USA, 2013. [CrossRef]

39. Linares, J.I.; Montes, M.J.; Cantizano, A.; Sánchez, C. A novel supercritical CO2 recompression Brayton power cycle for power tower concentrating solar plants. *Appl. Energy* **2020**, *263*, 114644. [CrossRef]